Zhang *et al. Chem. Synth.* **2025**, *5*, 25
DOI: 10.20517/cs.2024.115

Chemical Synthesis

Research Article

Open Access

Selective photooxidation of 5-hydroxymethylfurfural in water enabled by highly dispersed gold nanoparticles on graphitic carbon nitride

Qizhao Zhang[1], Botao Fan[1], Yuxi Wang[1], Bang Gu[1,*], Qinghu Tang[2], Feng Qiu[3], Qiue Cao[1], Wenhao Fang[1,*]

[1]School of Chemical Science and Technology, Yunnan University, Kunming 650091, Yunnan, China.
[2]School of Chemistry and Chemical Engineering, Collaborative Innovation Center of Henan Province for Green Manufacturing of Fine Chemicals, Key Laboratory of Green Chemical Media and Reactions - Ministry of Education, Henan Normal University, Xinxiang 453007, Henan, China.
[3]National Center for International Research on Photoelectric and Energy Materials, School of Materials and Energy, Yunnan University, Kunming 650091, Yunnan, China.

Correspondence to: Dr. Bang Gu and Prof. Wenhao Fang, School of Chemical Science and Technology, Yunnan University, 2 North Cuihu Road, Kunming 650091, Yunnan, China. E-mail: gubang@ynu.edu.cn; wenhao.fang@ynu.edu.cn

How to cite this article: Zhang, Q.; Fan, B.; Wang, Y.; Gu, B.; Tang, Q.; Qiu, F.; Cao, Q.; Fang, W. Selective photooxidation of 5-hydroxymethylfurfural in water enabled by highly dispersed gold nanoparticles on graphitic carbon nitride. *Chem. Synth.* **2025**, *5*, 25. https://dx.doi.org/10.20517/cs.2024.115

Received: 30 Aug 2024 **First Decision:** 14 Oct 2024 **Revised:** 24 Oct 2024 **Accepted:** 1 Nov 2024 **Published:** 14 Feb 2025

Academic Editors: Shanshan Chen, Ying Wan **Copy Editor:** Ping Zhang **Production Editor:** Ping Zhang

Abstract

Photocatalytic synthesis of chemicals is highly recognized for its eco-friendliness and mild reaction conditions, yet it faces considerable challenges regarding catalytic efficiency, stability and cost. The selective photooxidation of 5-hydroxymethylfurfural to 2,5-diformylfuran in water is a cost-effective and sustainable route for biomass valorization. The capability of a photocatalyst to capture visible light is paramount for efficiently harnessing solar energy and is the most critical initial step. Therefore, metal nanocatalysts with visible-light response and localized surface plasmon resonance have received widespread attention. In this work, graphitic carbon nitride (g-C_3N_4) with different morphologies was synthesized through high-temperature calcination of various organic precursors. Following that, the photodeposition of Au nanoparticles was used to construct a Schottky junction photocatalyst endowed with the localized surface plasmon resonance effect. The optimal Au/CN(I) catalyst achieved a 26% yield of 2,5-diformylfuran and productivity of 72.7 $mg_{DFF}\ g_{catal.}^{-1}\ h^{-1}$ under simulated sunlight in oxygen and water without any additives. This outstanding result outperformed most g-C_3N_4 and metal oxide photocatalysts ever reported in the literature. The interfacial electronic interactions between Au nanoparticles and g-C_3N_4 semiconductors were meticulously elucidated using comprehensive characterizations and computational

calculations. The roles of different reactive oxygen species were clarified by a series of controlled experiments. A plausible mechanism explaining the origin of visible-light response and photocatalytic performance was discussed.

Keywords: Photocatalysis, 2,5-diformylfuran, visible light, localized surface plasmon resonance, schottky junction, green synthesis

INTRODUCTION

Lignocellulosic biomass constitutes the most abundant renewable carbon resource on our planet and stands at the forefront of sustainable energy and chemical production[1,2]. With an ever-transforming global energy landscape and a growing emphasis on environmental sustainability, the efficient conversion of biomass into valuable chemicals has become a critical area of focus within scientific research and industrial development[3-5]. One such endeavor involves the catalytic transformation of 5-hydroxymethylfurfural (HMF), a versatile platform molecule derived from biomass, into 2,5-diformylfuran (DFF)[6,7]. This is a high-value compound with significant potential in the synthesis of furan-based polymers, organic conductors and synthetic intermediates for pharmaceuticals and antifungal agents[7].

The photocatalytic selective oxidation of HMF to DFF represents a significant advancement in the field, offering a pathway to more efficient and environmental benign processes[8]. This approach not only addresses the scientific challenges associated with selective oxidation but also aligns with the commercial potential for manufacturing high-performance materials and chemicals. By integrating cutting-edge photocatalytic techniques with a deep understanding of the underlying reaction mechanisms, this work aims to pave the way for innovative applications in catalytic science and sustainable chemistry, as supported by a comprehensive review[8,9] of the literature and our experimental findings[10-15].

The oxidation of HMF remains a significant challenge in the chemical industry because traditional processes often rely on hazardous oxidants and harsh reaction conditions[16,17]. Alternatively, photocatalytic oxidation of HMF has emerged as a green and low-power approach, being capable of harvesting solar energy under mild conditions[8,18,19]. In this context, graphitic carbon nitride (g-C_3N_4) can distinguish itself as a premier photocatalyst due to its unique electronic structure, optimal bandgap (*ca.* 2.7 eV) and exceptional stability[20]. These features allow collective enhancement of light absorption and photocatalytic efficiency across the visible spectrum. The superiority of g-C_3N_4 is underscored by its selectivity in generating singlet oxygen ($^1O_2$) over the indiscriminate hydroxyl radical (·OH), thereby mitigating unexpected over-oxidation of target molecules[21]. However, the intrinsic activity of g-C_3N_4 is limited due to the low utilization of visible light and the recombination of photogenerated electrons (e^-) and holes (h^+).

Despite its promising properties, optimizing g-C_3N_4 for enhanced photocatalytic performance necessitates addressing the efficiency of charge-carrier separation and transport. Thus, many efforts have been made through structural modification, element doping, heterojunction construction, and co-catalyst integration[20]. However, the reported superior separation and transfer of photogenerated charge carriers must use harmful organic solvents like trifluoromethylbenzene[22]. Therefore, the demand for greener synthetic protocols calls for environmentally friendly solvents, especially the cleanest water solvents. In the literature, thermal exfoliation[23] and H_2O_2 complexation[24-26] have been tried to improve the catalytic performances of g-C_3N_4 for photooxidation of HMF to DFF in the aqueous phase, but the obtained catalytic efficiencies are dissatisfying. As a result, new strategy is still needed to significantly boost the g-C_3N_4 catalysis for this target reaction.

Metal nanocatalysts with visible-light response and localized surface plasmon resonance (LSPR) have received widespread attention[27]. Plasmonic metal nanostructures have the capacity to augment the photon-to-charge conversion efficiency within metal-semiconductor hybrid systems *via* working mechanisms such as direct electron transfer, resonant energy transfer, and the expedited separation of excitons[28]. These phenomena are generally interpreted by the traditional model of plasmon-induced hot electron transfer (PHET), where hot carriers are initially produced in the metal through plasmonic decay before transitioning to molecular or semiconductor acceptors at the interface[29]. In metal-semiconductor junctions, effective interfacial transfer of hot electrons requires enough high energy to go upper the conduction band edge of a semiconductor and possesses adequate momentum to traverse the interface. Moreover, a swift rate of interfacial hot electron transfer (HET) is imperative to contend with the rapid relaxation process of hot carriers on metals[30]. As a result, for typical plasmonic metals such as Au, Ag and Cu, the relatively modest initial energy of hot electrons coupled with the rivalry between interfacial transfer and the swift relaxation of hot carriers restricts the overall efficiency of the PHET process[31]. Unfortunately, only a few studies have been devoted to coupling *g*-C_3N_4 with Au and Pd plasmonic metals for photochemical conversion of furfural-based biomass, *i.e.*, a Ni-Au/CN catalyst for photooxidation of furfuryl alcohol[32] to furfural and a Pd@E-*g*-C_3N_4 catalyst for photoreduction of furfural to γ-butyrolactone[33]. To the best of our knowledge, there has been no report to date on Au/*g*-C_3N_4 catalyst with the LSPR effect for photooxidation of HMF. More importantly, the electronic interaction mechanism between a noble metal and *g*-C_3N_4, as well as the relationship between the LSPR effect and the PHET process, remains obscure.

Herein, this work is devoted to improving the pristine photocatalytic efficiency of *g*-C_3N_4 by *in situ* deposition of Au nanoparticles so as to create the LSPR effect. The origin of different catalytic results, which depend on the *g*-C_3N_4 morphology and Au size, is unraveled. This innovative strategy can bolster not only the catalyst response to visible light but also its selectivity toward DFF. Furthermore, this study delves into the real reactive oxygen species, the interfacial electron transfer processes, and reaction mechanism of this photocatalytic system. This work also reveals for the first time the relationship between the energy of photogenerated e^- obtained from the LSPR effect of noble-metal nanoparticles and their ability to migrate to semiconductors. This can provide a valuable reference for future research on plasmonic metal/*g*-C_3N_4 type photocatalysts.

EXPERIMENTAL

Materials

Urea (99.5%), dicyandiamide (99%) and gold (III) chloride trihydrate (99.9%, Au 50%) from Innochem, and methanol (AR, 99.5%) and melamine (99%) from Aladdin were used for catalyst preparation. HMF (98%), DFF (98%), 5-hydroxymethyl-2-furoic acid (HMFCA, 98%), 5-formyl-2-furoic acid (FFCA, 98%) and 2,5-furan dicarboxylic acid (FDCA, 98%) from Ark Pharm were used for catalytic reactions and quantitative analysis.

Catalyst preparation

The overall synthetic method was described in Supplementary Scheme 1. *g*-C_3N_4 was prepared with three different precursors by high-temperature calcination. In a typical procedure, urea, dicyandiamide or melamine was placed in a ceramic crucible with the lid to ensure a certain degree of sealing. The calcination was carried out from room temperature to 550 °C (2 °C min^{-1}) and maintained for 4 h. The solids were then cooled naturally to room temperature and ground for 30 min. The so-obtained *g*-C_3N_4 carrier was named CN(I), CN(II) and CN(III), respectively.

g-C_3N_4 supported Au catalyst (loading: 1 wt%) was prepared using photodeposition method. Typically, 250 mg of *g*-C_3N_4 was dispersed in 100 mL of deionized water, followed by adding 50 mL of methanol and 0.5 mL of Au solution (5 mg mL^{-1}). Then, the mixture was sonicated for 5 min and irradiated under a Xe lamp (300 W) for 1 h. Afterward, the solids were filtrated with deionized water and dried at 80 °C overnight. The as-prepared Au catalyst was named Au/CN(I), Au/CN(II) and Au/CN(III), respectively.

Catalyst characterizations

Physical characterizations

Inductively-coupled-plasma mass spectrometry (ICP-MS) was carried out using an Agilent 7500a apparatus. Powder X-ray diffraction (XRD) analysis was performed on a Bruker D8 Advance diffractometer by utilizing Cu Kα radiation at a beam voltage of 40 kV. The diffraction pattern was scanned with a rate of 0.1° s^{-1}. N_2 physisorption measurement was done at 77 K using a Micromeritics TriStar II 3020 Surface-Area Analyzer. The Brunauer-Emmet-Teller (BET) and Barrett-Joyner-Halenda (BJH) models were applied for calculating specific surface area and pore size distribution, respectively. Transmission electron microscopy (TEM) and energy-dispersive X-ray spectroscopy (EDS) analyses were performed on a JEOL JEM-F200 filed-emission electron microscope with an acceleration voltage of 200 kV. The average size of Au particles was estimated by measuring one hundred particles. An atomic force microscope (AFM) image was obtained on a Bruker MultilMode 8 apparatus. The photoluminescence (PL) spectrum was obtained using an Edinburgh Instrument FSL980 by spanning a steady-state spectrum from 200 to 1,700 nm with the excitation wavelength fixed at 480 nm. X-ray photoelectron spectroscopy (XPS) was conducted on a Thermo Scientific Kα + system with Al Kα radiation under ultrahigh vacuum with spectra calibrated for surface charging using the C 1s line at 284.8 eV. Ultraviolet-visible diffuse reflectance spectroscopy (UV-vis DRS) was executed on a Shimadzu UV3600. Electron paramagnetic resonance (EPR) spectra were recorded on a Bruker A300 spectrophotometer. The spectra were obtained on solution samples (100 mmol L^{-1}), using 1-20 mW microwave power and 100 kHz field modulation with the amplitude set to 1 G. The *g*-values for each EPR spectrum were extracted from simulations performed using EasySpin (v5.2.23).

Photoelectrochemical characterizations

The photoelectrochemical (PEC) performance of catalyst was assessed using an AutoLab electrochemical workstation, model PGSTAT302N within a standard three-electrode configuration. The working electrode comprised Indium tin oxide (ITO) glass coated with the catalyst, a saturated calomel electrode (SCE) functioned as the reference, and a platinum wire served as the counter electrode. To prepare the working electrode, 5 mg of the catalyst was dispersed with 0.5 mL of ethanol, to which 10 μL of Nafion® solution was added, followed by 2 h of sonication. To prepare the thin-film electrode, 10 μL of the mixture was finely applied onto ITO glass with an area of 0.25 cm^2, followed by drying at room temperature for 30 min. The PEC measurement was conducted at 25 °C under a 300 W Xe lamp with a Na_2SO_4 electrolyte solution (0.5 mol L^{-1}, pH = 6.8).

Catalyst evaluation

As illustrated in Supplementary Scheme 2, the aqueous phase aerobic oxidation of HMF to DFF was conducted under atmospheric pressure at a fixed temperature of 35 °C in a quartz reactor. Typically, HMF (0.1 mmol), catalyst (30 mg) and deionized water (100 mL) were mixed into the reactor, which was then subjected to an ultrasonic treatment at 40 kHz for 15 min to ensure complete dissolution and dispersion, followed by stirring in the dark at 500 rpm for an additional 15 min to achieve desorption equilibrium between the catalyst and the reactant.

For the photochemical reaction, a Xe lamp (CEL-HXF300-T3 provided by Beijing China Education Au-light Technology Co., Ltd.) emitting light in the range of 350-780 nm at an intensity of 0.75 W cm^{-2} was used. The Xe lamp was placed vertically 6 cm above the liquid surface and the reactor was connected to a thermostat water at 35 °C and an O_2 flow of 10 mL min^{-1}. The continuous sampling with 0.5 mL aliquots was conducted every 15 min. The quantitative analysis was carried out on an Agilent 1260 Infinity HPLC system using external standard method and diluted H_2SO_4 solution (5 mmol L^{-1}) as mobile phase. The photodiode array detector (DAD) and the Shodex SH-1011 sugar column (8 mm, 300 mm, 6 μm) were configured. The specific wavelengths were set for detecting HMF (285 nm), DFF/FFCA (290 nm), and HMFCA/FDCA (260 nm). To ensure the data reproducibility, each reaction was performed at least twice. The conversion of HMF, selectivity of product, yield and productivity of DFF were calculated based on the carbon balance, as determined by

$$\text{Conv.}(\%) = \frac{n_{\text{HMF,initial}} - n_{\text{HMF,final}}}{n_{\text{HMF,initial}}} \tag{1}$$

$$\text{Select.}(\%) = \frac{n_{\text{product}}}{n_{\text{HMF,initial}} - n_{\text{HMF,final}}} \tag{2}$$

$$\text{Yield}(\%) = \frac{n_{\text{DFF}}}{n_{\text{HMF,initial}}} \tag{3}$$

$$\text{Prod.}\left(\text{mg}_{\text{DFF}}\ \text{g}_{\text{catal.}}^{-1}\ \text{h}^{-1}\right) = \frac{W_{\text{DFF}}}{W_{\text{catal.}} \times \text{reaction time}} \tag{4}$$

Density functional theory calculations

Density functional theory (DFT) calculations were performed using the Vienna Ab initio Simulation Package (VASP)[34]. The elemental core and valence electrons were represented by the projector augmented wave (PAW) method and plane-wave basis functions with a cut-off energy of 500 eV. For all the calculations, generalized gradient approximation with the Perdew-Burke-Ernzerhof (GGA-PBE) exchange-correlation functional was employed. The DFT-D3 empirical correction method was used to describe van der Waals interactions. Monkhorst-Pack k-points of 2 × 2× 1 were applied. All structures were optimized without constraint with a force tolerance of 0.02 eV $Å^{-1}$. The *g*-C_3N_4 model was built according to the literature[35]. For the Au/CN(I) catalyst, ten Au atoms were stacked on the (111) crystal plane above the (001) crystal plane of the *g*-C_3N_4 model.

RESULTS AND DISCUSSION

Firstly, the Au content of the catalyst was determined by ICP-MS. The precise loadings are all around 1 wt% [Supplementary Table 1], showing the effective immobilization of Au onto carriers. The composition and phase structure of the as-synthesized catalytic materials were later examined by XRD. Figure 1A illustrates a typical XRD pattern due to *g*-C_3N_4 for all the solids. The characteristic peaks at 13.1° and 27.5° correspond to the (100) and (002) planes of *g*-C_3N_4, which results from the interlayer stacking of the conjugated aromatic system[36]. This observation verifies the successful construction of analogous *g*-C_3N_4 structure by even using different organic precursors through calcination. In addition, Figure 1A shows new diffraction peaks at 38.3°, 44.4° and 64.6° for Au/CN(II) and Au/CN(III), which can be attributed to the (111), (200) and (220) planes of Au (PDF #89-3697)[32]. The mean Au size calculated by the Scherrer equation is approximately 6.7 and 7.5 nm [Supplementary Table 1], respectively. However, these typical Au peaks are not detected on the Au/CN(I) catalyst, which could originate from the highly dispersed Au particles with small sizes. This interesting phenomenon indicates that the properties of different *g*-C_3N_4 carriers can affect the particle size of supported Au.

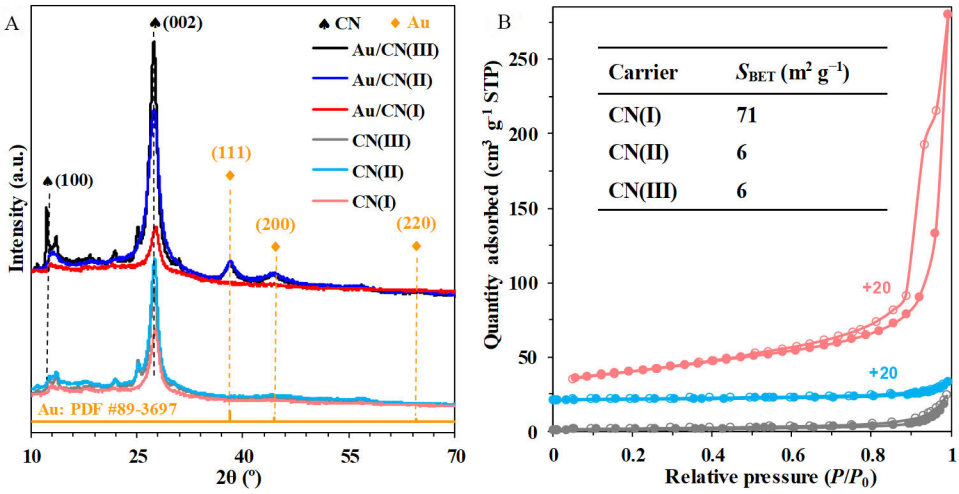

Figure 1. (A) XRD patterns of g-C_3N_4 carriers and supported Au catalysts; (B) N_2 isothermal curves and pore size distribution of g-C_3N_4 carriers. XRD: rowder X-ray diffraction.

Afterward, the porosity of the bare carriers was analyzed by N_2 adsorption-desorption. As depicted in Figure 1B, all the g-C_3N_4 carriers display type-IV isotherms but only CN(I) presents an obvious type-H3 hysteresis loop at a high P/P_0 of 0.6-0.9. This isothermal feature usually reflects irregular mesoporous structure due to the stacking of layered materials[37]. As a result, CN(I) exhibits a much higher specific surface area of 71 m^2 g^{-1}, reaching *ca.* 12 folds over that of CN(II) and CN(III) (6 m^2 g^{-1}). This significant difference in surface area can be responsible for the high dispersion of Au nanoparticles on the CN(I) carrier. As is well known, carbon nitride materials are constructed on melem units, specifically pyrolysis of urea, dicyandiamide and melamine to melem requires three-step, two-step and one-step thermal polymerization, respectively[36]. Therefore, the polymerization degree of the as-prepared g-C_3N_4 carriers from the three precursors is CN(I) < CN(II) < CN(III)[23]. As a result, the different polymerization degrees of g-C_3N_4 due to various building blocks can decide the final morphology.

Following that, the morphology of the Au catalyst was further inspected by TEM, AFM, and EDS. The TEM images reveal the distinct structural features of Au nanoparticles loaded on different g-C_3N_4 carriers. Specifically, CN(I) obtained through urea pyrolysis displays a single-layered flake-like structure [Figure 2A], while CN(II) derived from dicyandiamide pyrolysis presents a multi-layered structure with flake-like stacking [Figure 2B]. However, CN(III) resultant from melamine pyrolysis mainly exhibits nanorod-like structure [Figure 2C]. Moreover, the supported Au nanoparticles are found to continuously grow bigger and become aggregated. The average sizes of Au are estimated to be *ca.* 5.6, 8.7 and 11 nm for the Au/CN(I), Au/CN(II) and Au/CN(III) catalysts, respectively. These values are similar to the Au sizes measured by the XRD technique. Notably, AFM measurement further proves the single-layered flake structure of CN(I) [Figure 2D]. This feature allows effective dispersing of Au nanoparticles onto the large surface of CN(I), giving uniform and small Au sizes. On the contrary, the multi-layered nanosheet and nanorod structures with extremely small surface areas would eventually result in embedding and aggregating of Au nanoparticles on CN(II) and CN(III). A high-resolution TEM image confirms the formation of Au crystals. The interplanar spacing of 0.235 nm can be identified to be the (111) plane of cubic Au[38]. Furthermore, EDS analysis clearly visualizes the elemental composition and distribution. The uniform overlapping of C and N elements substantiates the successful synthesis of carbon nitride [Figure 3]. The Au sizes and particle dispersions on g-C_3N_4 are very well coincident with XRD and TEM results.

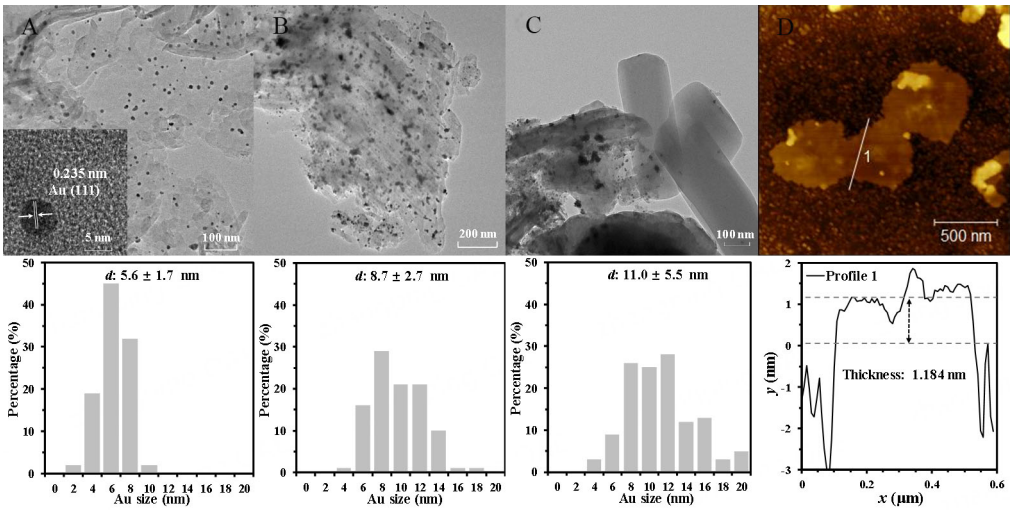

Figure 2. TEM images and the estimated size distribution of Au nanoparticles for the (A) Au/CN(I); (B) Au/CN(II), and (C) Au/CN(III) catalysts; (D) AFM image and analysis of Au/CN(I). TEM: transmission electron microscopy; AFM: an atomic force microscope.

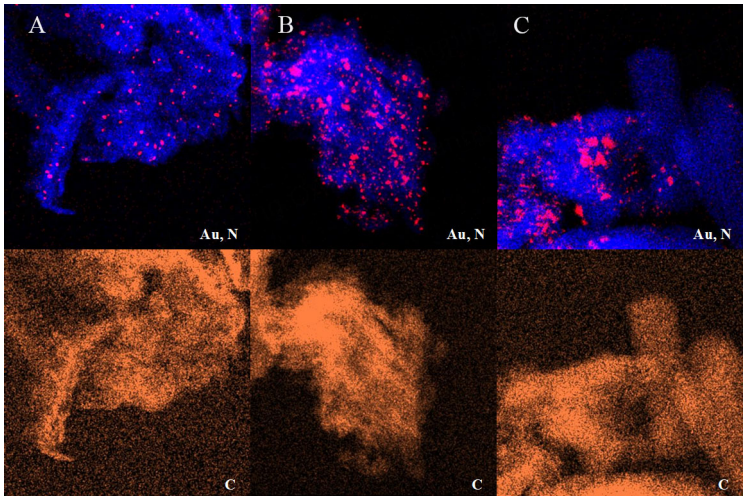

Figure 3. Color-coded elemental maps of Au from the M line, N from the K line and C from the K line for the (A) Au/CN(I); (B) Au/CN(II), and (C) Au/CN(III) catalysts.

The visible-light-driven photocatalytic oxidation of HMF to DFF was first investigated using different g-C_3N_4 carriers after 120 min of irradiation. Figure 4A shows that CN(I) bearing single-layered flake architecture and the largest specific surface area can reach the highest conversion of HMF (81%) and selectivity of DFF (23%). However, CN(II) and CN(III) display deficiencies either in conversion or selectivity. Upon the deposition of Au nanoparticles, enhanced HMF conversion (84%) and DFF selectivity (28%) are only attained by using the Au/CN(I) catalyst [Figure 4A]. As a result, the yield of DFF accordingly increases from 18% to 24%. Meanwhile, Au/CN(II) and Au/CN(III) exhibit a decreased conversion but with an increased selectivity, leading to obviously declined DFF yield at 20% and 14%, respectively. This disparity may stem from the modified energy band of the catalyst due to co-influence of Au size and g-C_3N_4 properties.

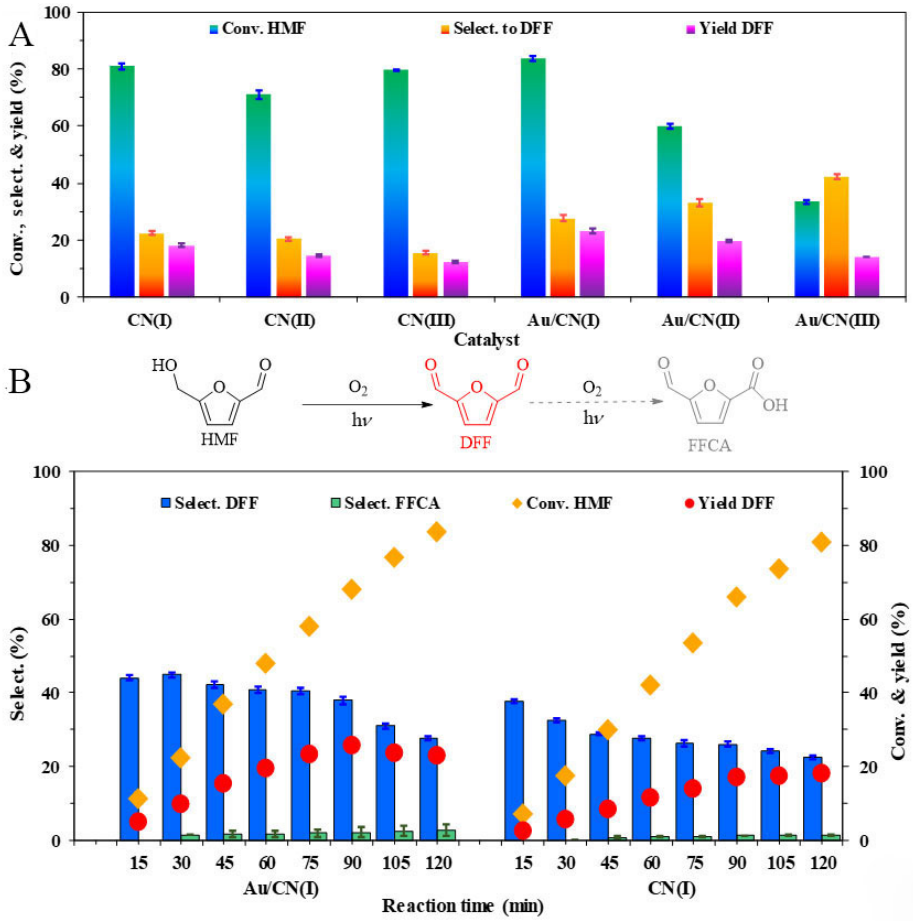

Figure 4. (A) Catalytic performances of g-C_3N_4 carriers and supported Au catalysts for photooxidation of HMF to DFF; (B) Time-course investigation of CN(I) and Au/CN(I) during photooxidation of HMF. Reaction conditions: HMF, 0.1 mmol; catalyst, 30 mg; deionized water, 100 mL; O_2 flow, 10 mL min^{-1}; Xe lamp, l = 350-780 nm; temperature, 35 °C; time, 2 h for (A). HMF: 5-hydroxymethylfurfural; DFF: 2,5-diformylfuran.

Thereafter, the evolution of HMF conversion and product selectivity was compared between CN(I) and Au/CN(I) by using a time-dependent experiment. As depicted in Figure 4B, Au/CN(I) enables not only slightly increased HMF conversion but also significantly improved DFF selectivity during the whole reaction, in comparison with CN(I) performance. After 90 min of irradiation, the yield of DFF achieves the optimum of 26% on the Au/CN(I) catalyst, reaching 1.5-fold higher than that of the CN(I) carrier. This result could reasonably originate from the LSPR effect of Au nanoparticles, which boosts the visible light response and photon charge conversion efficiency of CN(I) carriers. With the time on stream, the selectivity of DFF gradually declines with formation of a small amount of FFCA. This phenomenon implies the accumulation of different reactive oxygen species in the photocatalytic system, some of which may overoxidize DFF to FFCA.

In order to compare the catalyst efficiency among different g-C_3N_4-based catalysts in the literature, the productivity of DFF defined as $mg_{DFF}\ g_{catal.}^{-1}\ h^{-1}$ for a catalyst was calculated to quantify the activity of g-C_3N_4 for producing DFF in a unit time. As summarized in Table 1, the present Au/CN(I) catalyst demonstrates a 26% yield of DFF, placing it among the top catalysts working in the aqueous phase. More importantly, the productivity of DFF over the Au/CN(I) catalyst reaches as high as 72.7 $mg_{DFF}\ g_{catal.}^{-1}\ h^{-1}$, being the most active catalyst reported in the literature to date. This outstanding efficiency has surpassed over three times the

Table 1. Comparison of catalytic performances of g-C_3N_4-based catalysts for photooxidation of HMF to DFF in water under simulated sunlight

Catalyst	Prod. DFF ($mg\ g^{-1}\ h^{-1}$)	Conv. HMF (%)	Select. DFF (%)	Yield DFF (%)	Ref.
ZnPp-C_3N_4-TE	6.2	73	36	26	[39]
US-$CHNO_3$	8.4	80	22	18	[21]
PCN-H_2O_2	8.7	21	88	18	[25]
PCN-H_2O_2	12.4	47	71	33	[24]
MCN-TE-H_2O_2	21.6	26	88	23	[26]
g-C_3N_4(MCN)	22.9	>99	49	49	[23]
Au/CN(I)	72.7	68	38	26	This work

DFF: 2,5-diformylfuran; HMF: 5-hydroxymethylfurfural.

highly active benchmark catalysts, *i.e.*, polymeric carbon nitride obtained by thermal etching and adducted with hydrogen peroxide (MCN-TE-H_2O_2, 21.6 $mg_{DFF}\ g_{catal.}^{-1}\ h^{-1}$)[26] and g-C_3N_4 derived from melamine and thermally exfoliated at 540 °C for 4 h [g-C_3N_4 (MCN), 22.9 $mg_{DFF}\ g_{catal.}^{-1}\ h^{-1}$][23]. Besides, the Au/CN(I) catalyst can even outperform the classic TiO_2-based and Bi-based semiconductors which are well-known as highly efficient catalysts for photooxidation of HMF [Supplementary Table 2][8].

To delve deeper into the remarkable boost in photocatalytic activity conferred by the interfacial interactions between Au nanoparticles and g-C_3N_4, a series of characterizations were performed. UV-vis DRS was first employed to scrutinize the light absorption capability of solids. Figure 5A illustrates that different g-C_3N_4 carriers can absorb light in the partial visible and ultraviolet regions and CN(I) exhibits the most robust absorption. This absorption capability can be obviously improved by dispersing small-sized Au nanoparticles onto g-C_3N_4. Notably, the absorption of visible light is greatly enhanced on Au/CN(I). This phenomenon has been largely attributed to the LSPR of Au nanoparticles in the literature[27].

Then, the bandgap energy (E_g) of the catalyst was extracted from the Tauc plot. As shown in Figure 5B, g-C_3N_4 supported Au catalysts display a lowered E_g compared to the carrier alone, which can be caused by the band bending of g-C_3N_4 semiconductors due to Au interaction. Furthermore, the absorption range of photon energy for the resonant Au nanoparticles on the Au/CN(I), Au/CN(II), and Au/CN(III) catalysts is determined to be 1.51, 1.35, and 1.25 eV, respectively. This variation can closely correlate with the growing size effect of Au nanoparticles[31].

Afterward, photocurrent measurement was conducted to assess the ability of a catalyst to provide photogenerated electrons after light absorption. As expected, Figure 5C shows a notable increase in photocurrent intensity for the CN(I) and CN(II) carriers with the presence of Au nanoparticles. On the contrary, a decreased photocurrent is obviously recorded on the Au/CN(III) catalyst compared to CN(III). This abnormal phenomenon may explain the sharp decline in HMF conversion on CN(III) due to Au deposition.

As is known to all, the strength of oxidation capability of a photocatalyst is intricately tied to its valence band position. Following that, valence band (VB)-XPS and Mott-Schottky analysis were used to investigate this important property[10]. As displayed in Supplementary Figure 1 and Supplementary Table 3, all the solids present positive slope curves, which are characteristic of n-type semiconductor behavior. The flat-band potentials [*i.e.*, Fermi levels (E_f)] measured against the SCE for CN(I), CN(II), CN(III), Au/CN(I), Au/CN(II) and Au/CN(III) are -0.80, -0.87, -0.91, -0.98, -0.91 and -0.92 V, respectively. Accordingly, the E_f

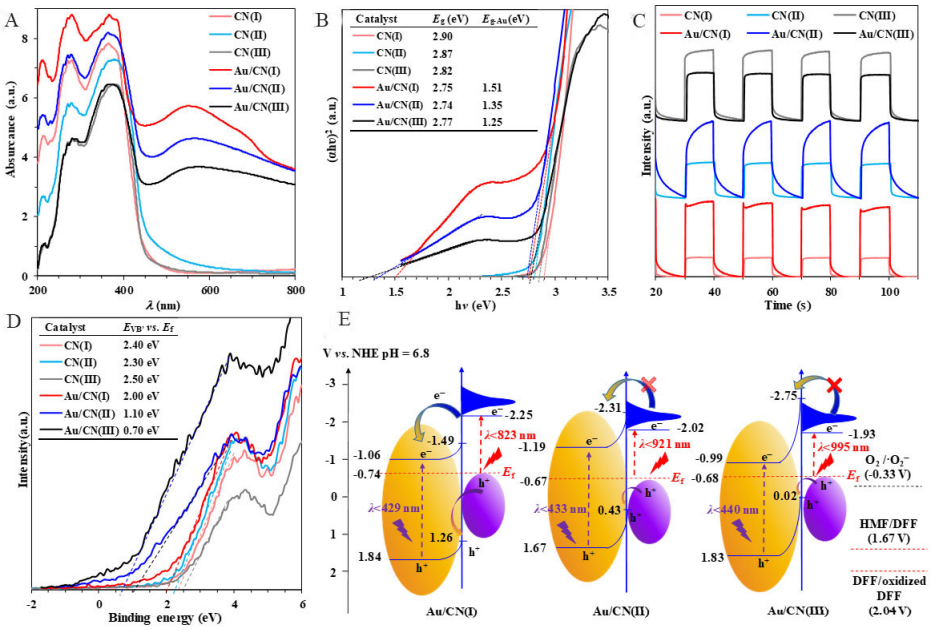

Figure 5. (A) UV-vis DRS; (B) Tauc plot; (C) photocurrent and (D) VB-XPS of g-C_3N_4 carriers and supported Au catalysts; (E) Schematic diagram of the band structure of the Au/CN(I), Au/CN(II), and Au/CN(III) catalysts. XPS: X-ray photoelectron spectroscopy.

values of these solids in reference to the normal hydrogen electrode (NHE) are calculated to be -0.56, -0.63, -0.67, -0.74, -0.67 and -0.68 V. As illustrated in Figure 5D, the differences in relative energy between the E_f and the valence band edge ($E_{VB'}$) for the photocatalysts are 2.40, 2.30, 2.50, 2.00, 1.10 and 0.70 eV, respectively. As listed in Supplementary Table 3, the valence band positions are subsequently determined to be 1.84, 1.67, 1.83, 1.26, 0.43 and 0.02 V *vs.* NHE. Thereby, the corresponding conduction band positions are calculated to be -1.06, -1.20, -0.99, -1.49, -2.31 and -2.75 V *vs.* NHE. Based on UV-vis DRS results, the light absorption edges of Au nanoparticles are found to be 1.51, 1.35, and 1.25 eV [Figure 5B], respectively. Therefore, it can be concluded that the oxidation-reduction potentials of photogenerated e^- on Au nanoparticles of Au/CN(I), Au/CN(II) and Au/CN (III) through LSPR effect are -2.25, -2.02, and -1.93 V *vs.* NHE. As shown in Figure 5A-B, a new absorption peak at *ca.* 560 nm emerges after deposition of Au onto g-C_3N_4. This observation implies the origin of this absorption behavior due to the LSPR effect of Au nanoparticles. As a consequence, the absorption edge of this peak aligns with the energy of the photogenerated e that is harvested by Au nanoparticles *via* the LSPR effect. These findings demonstrate that the combination of *in situ* grown Au nanoparticles with g-C_3N_4 can lead to a higher propensity for electron transfer from g-C_3N_4 semiconductors to Au due to the metal's substantial work function. In addition, the optimal Au/CN (I) catalyst exhibits the strongest photocurrent intensity and the greatest amplification before and after loading with Au nanoparticles [Supplementary Figure 2]. Therefore, this catalytic property gives rise to the upward band bending and the formation of Schottky junction at the interface between Au nanoparticles and g-C_3N_4 semiconductors[40].

As displayed in Figure 5A, there is an inverse relationship between supported-Au size and visible-light response. This correlation can be attributed to the enhanced LSPR effect that occurs with decreasing metal particle size. Furthermore, Figure 5E illustrates that the energy barrier at the Schottky junction, which is formed by the bending of the energy bands upon the combination of a semiconductor and a metal, also diminishes as the Au size decreases. Consequently, the reduced size of Au nanoparticles facilitates the mobility of photogenerated e^- through LSPR effect, crossing the energy barrier of the Schottky junction.

Such an ease of traversal can promote the migration of those photogenerated e^-.

Based on the above results, Figure 5E illustrates that the energy of photogenerated electrons excited by the LSPR effect on the Au/CN(I) catalyst can significantly exceed the Schottky barrier[28]. In contrast, the energies for the Au/CN(II) and Au/CN(III) catalysts fall short with the latter being substantially insufficient. As a consequence, the Au/CN(I) catalyst enables swift migration and separation of photogenerated e^- and h^+ between the metal and semiconductor. However, the Au/CN(III) catalyst fails to achieve this separation process, which eventually culminates in a reduced photocurrent intensity.

As shown in Supplementary Figure 3A, CN(I) demonstrates the lowest fluorescence intensity relative to CN(II) and CN(III), which means the minimal recombination rate of photogenerated e^- and h^+ for the CN(I) catalyst. After photodeposition of Au nanoparticles, the photoresponse intensity of CN(I) obviously increases but the fluorescence intensity further decreases. This clearly illustrates that Au nanoparticles can enhance the separation of photogenerated charge carriers. Furthermore, electrochemical impedance spectroscopy (EIS) experiments show declining impedances for all *g*-C_3N_4 carriers after introducing Au [Supplementary Figure 3B][10]. This trend implies that the *in situ* formed Au nanoparticles can lower the resistance to electron transfer, thus facilitating the migration of photogenerated electrons across the catalyst surface. The Au/CN(I) catalyst exhibits the smallest Nyquist radius, which is indicative of the most efficient generation, separation and transfer of photogenerated e^- and h^+.

To further elucidate the electron transfer and band structure alteration between Au nanoparticles and the CN(I) carrier, DFT calculations were executed. Figure 6A and B illustrates that the valence band maximum and conduction band minimum of CN(I) are mainly constituted by the 2p orbitals of C and N. Under light exposure, the electron transition from the C 2p to the N 2p orbitals enables the generation of photoinduced e^- and h^+. The incorporation of Au nanoparticles notably narrows the bandgap and the valence band maximum is found predominantly by contribution of the 5d orbital of Au. This result indicates that electrons upon absorbing photon energy can move from the Au 5d orbital to the N 2p orbital within the Au/CN(I) catalyst.

Moreover, differential charge density distribution calculations were used for verifying the electron transfer. As shown in Figure 6C, yellow and green patterns represent the electron-sufficient and electro-deficient regions, respectively. The scheme clearly illustrates electron transfer from CN(I) to Au. XPS analysis discloses the presence of predominant Au species in a metallic state on the surface of Au/CN(I) catalyst [Supplementary Figure 4]. This shows that photodeposition method enables formation of metallic Au nanoparticles on CN(I) from *in situ* reduction of Au^{3+} salt. The C 1s spectrum of CN(I) can be resolved into three peaks at 284.4, 286.1 and 288.3 eV [Supplementary Figure 5], which can be ascribed to carbon species in the C-C, C-O and N=C-N functional groups of *g*-C_3N_4, respectively. Notably, the binding energies of those carbon species are found to remain unchanged after Au deposition, suggesting a negligible interaction between Au and CN(I). On the other hand, deconvolution of the N 1s spectrum of CN(I) leads to three peaks at 398.9, 399.8 and 401.3 eV [Figure 6D], corresponding to the distinct N species in C-N=C, N-$(C)_3$ and C-N-H groups, respectively. After Au deposition, the peak for N-$(C)_3$ remains static while those for C-N-H and C-N=C groups shift to lower binding energies by 0.1 and 0.2 eV, respectively. This unique phenomenon can originate from the strong interaction during Au anchoring onto the C-N=C group, thus promoting electron transfer from N to Au. These evidences of elemental interactions on Au/CN(I) surface align well with the computational predictions, which confirm the electron transfer process and the subsequent formation of Au/CN(I) Schottky junction.

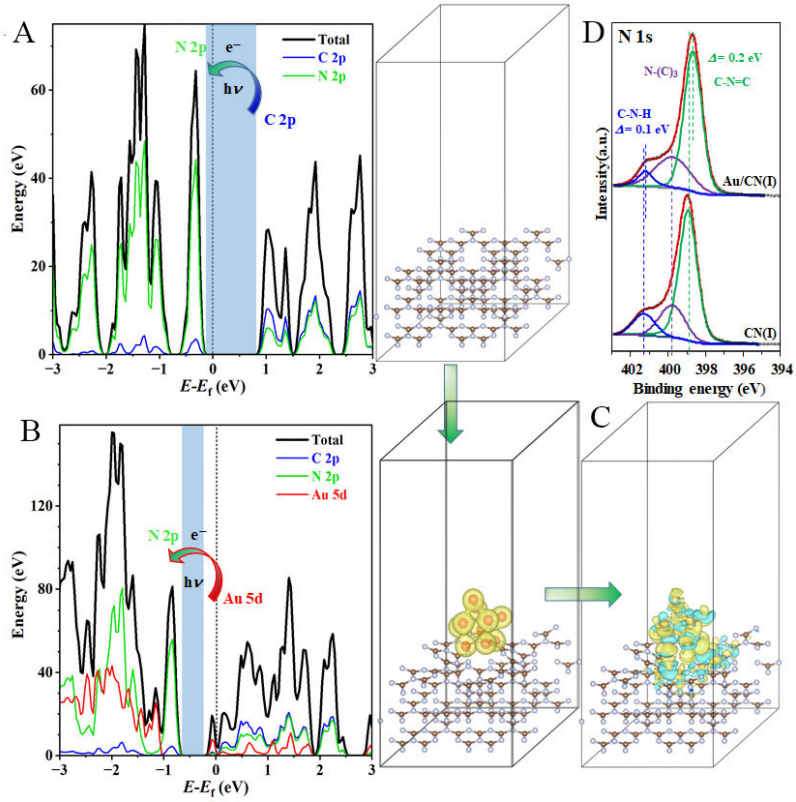

Figure 6. PDOS of the (A) CN(I) carrier and (B) Au/CN(I) catalyst; (C) Differential charge density distribution of Au/CN(I); (D) XPS spectra of N 1s core level of CN(I) and Au/CN(I). XPS: X-ray photoelectron spectroscopy.

The generation and transformation of reactive oxygen species are pivotal in photocatalytic oxidation reactions[41]. To identify the short-lived free radical intermediates in the reaction process, *in situ* EPR measurements were conducted. Typically, 2,2,6,6-tetramethyl-4-piperidinol (DMPO) is used as radical scavenger for hydroxyl radical (•OH) and superoxide anion ($•O_2^-$)[10] In addition, 2,2,6,6-tetramethylpiperidine (TEMP)[42] and 2,2,6,6-tetramethyl-1-piperidinyloxy (TEMPO)[43] are used as scavengers for singlet oxygen ($^1O_2$) and photogenerated h^+, respectively. Figure 7A-C shows almost no signals for •OH, $•O_2^-$ and $^1O_2$ under dark conditions but their EPR signals become visible and further grow intensive under light exposure within 1-10 min. These results can verify the *in situ* generation of these three radicals during HMF photooxidation using the Au/CN(I) catalyst. However, Figure 7D clearly displays a strong TEMPO signal in the dark but the signal significantly decreases upon illumination, showing h^+ generation.

Furthermore, the radical quenching experiments were carried out to understand the roles of different reactive oxygen species in determining activity and selectivity of the Au/CN(I) catalyst for HMF photooxidation. Typically, $AgNO_3$[44], benzoquinone (PBQ), triethanolamine (TEOA), 4-chloro-2-nitrophenol (4-C-2-NP)[42] and tertiary butyl alcohol (TBA)[10] are accordingly used as scavengers for photogenerated e^-, $•O_2^-$, h^+, $^1O_2$ and •OH. As shown in Figure 8A, O_2 molecules are verified to be essential for photooxidation of HMF. Without O_2, the catalytic performance of Au/CN(I) is largely inhibited. O_2 molecules can be transformed into $•O_2^-$ after reduction by e^- and $^1O_2$ after oxidation by h^+. It is disclosed that the addition of the corresponding PBQ and 4-C-2-NP scavengers allows a significant reduction of the catalytic performances. Yet, the addition of TBA for capturing •OH can hardly change the catalytic result. It

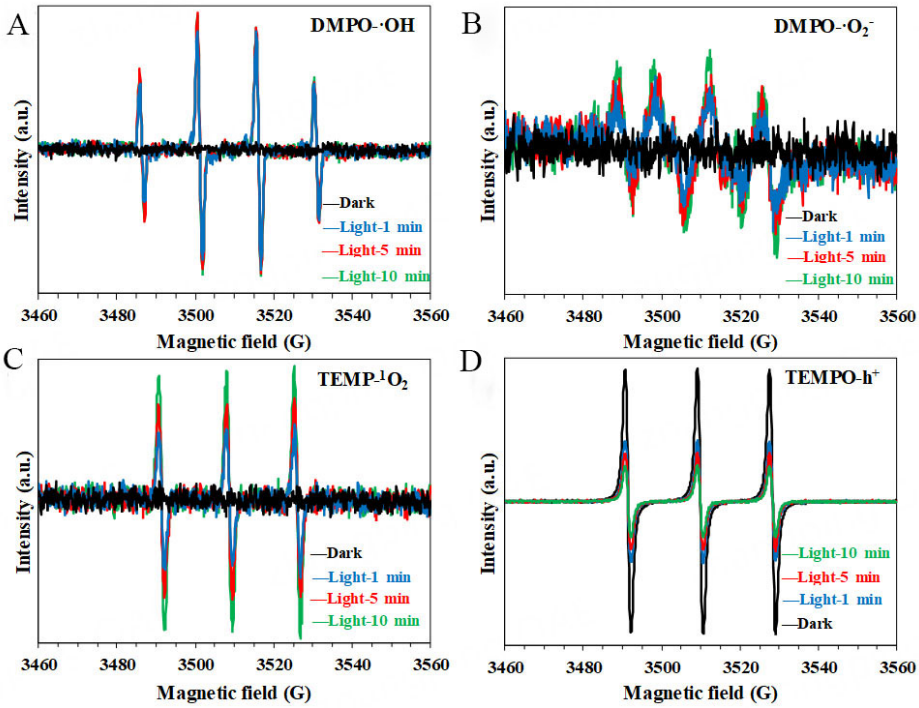

Figure 7. EPR *in situ* signals of (A) DMPO-·OH; (B) DMPO-·O_2^-; (C) TEMP-$^1O_2$, and (D) TEMPO-h^+ species during photooxidation of HMF with Au/CN(I) and water, except methanol for (B). EPR: electron paramagnetic resonance; DMPO: 2,2,6,6-tetramethyl-4-piperidinol; TEMP: 2,2,6,6-tetramethylpiperidine; TEMPO: 2,2,6,6-tetramethyl-1-piperidinyloxy; HMF: 5-hydroxymethylfurfural; EPR: electron paramagnetic resonance.

thus can be presumed that the generation of •OH in low concentration would not participate in the photocatalytic oxidation of HMF. Notably, the addition of TEOA for quenching h^+ greatly decreases conversion of HMF and selectivity of DFF. This shows that photogenerated h^+ can work as the most critical active species for Au/CN(I)-catalyzed photooxidation of HMF to DFF. Interestingly, the addition of $AgNO_3$ for e^- elimination can slightly promote conversion of HMF and selectivity of DFF, which demonstrates that over-oxidation of DFF can be mainly due to •O_2^-. That is because the captured e^- cannot recombine with h^+ and then h^+ can continuously generate and enrich on the catalyst surface. Meanwhile, the eliminated e^- can also inhibit •O_2^- formation from reductive activation of O_2. Therefore, it can be reasonably speculated that photogenerated h^+ initiate the oxidation of HMF by driving oxidative deprotonation to form alkoxyl radical and proton. At the same time, photogenerated e^- reduces O_2 to yield •O_2^- which subsequently reacts with the released proton to form hydroperoxyl radical (•OOH)[45]. This active species further oxidizes the alkoxyl intermediate to generate DFF and H_2O_2 byproduct, in agreement with the previous report[45]. Unfortunately, the presence of H_2O_2 can result in over-oxidation of DFF to FFCA and may even trigger the mineralization reaction. This is supported by the controlled experiment by using catalase as the scavenger for H_2O_2. As shown in Supplementary Figure 6, the selectivity of DFF is significantly improved with addition of catalase, verifying H_2O_2 byproduct to be an undesired oxidant during photooxidation of HMF.

After elucidation of the modification of band structure and the roles of different oxygen species, the plausible reaction mechanism of Au/CN(I)-catalyzed photooxidation of HMF to DFF can be discussed. As proposed in Figure 8B, highly dispersed Au nanoparticles with small sizes on CN(I) can give rise to electron transfer from Au to N, which causes the band bending and the formation of Schottky junction. The LSPR effect of Au nanoparticles enables the enhanced absorption of visible light, which allows excited electrons to

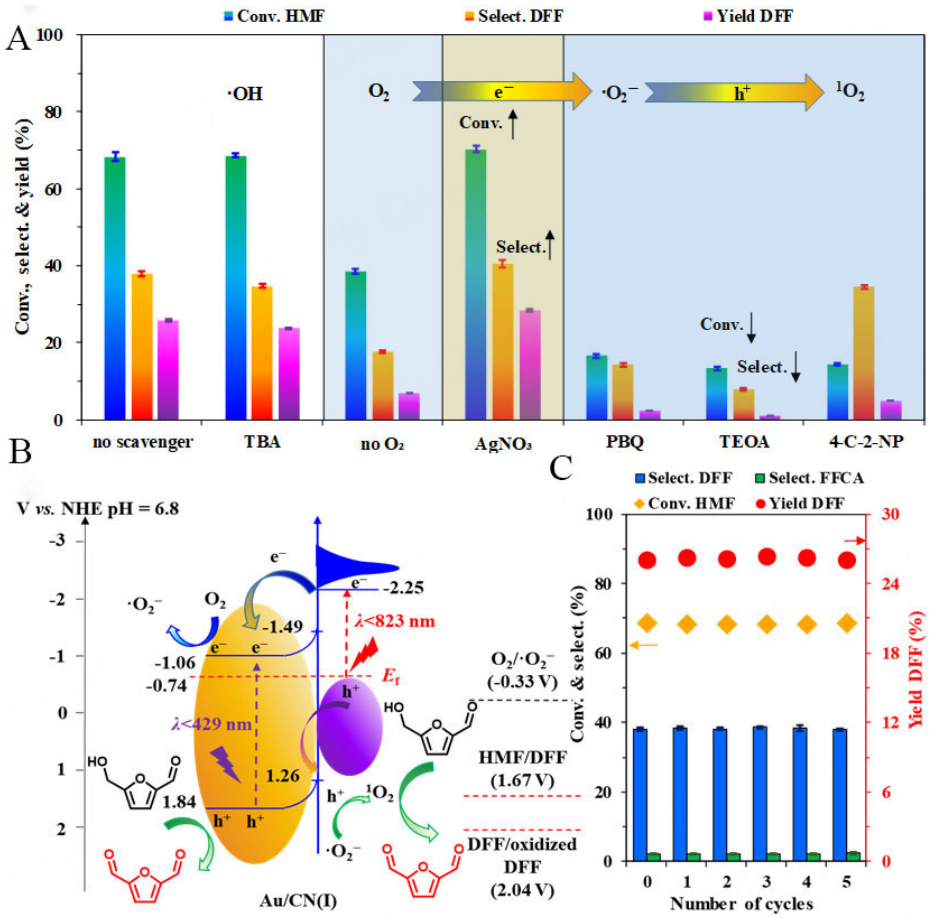

Figure 8. (A) Catalytic results of controlled experiments over the Au/CN(I) catalyst by adding different scavengers during photooxidation of HMF to DFF; (B) Plausible reaction mechanism of the photocatalytic oxidation of HMF to DFF using the Au/CN(I) catalyst; (C) Recycling test of the Au/CN(I) catalyst. Reaction conditions: HMF, 0.1 mmol; scavenger, 0.1 mmol; catalyst, 30 mg; deionized water, 100 mL; O_2 flow, 10 mL min^{-1}; Xe lamp, *l* = 350-780 nm; temperature, 35 °C; time, 1.5 h. HMF: 5-hydroxymethylfurfural; DFF: 2,5-diformylfuran.

overcome the Schottky barrier and move to the conduction band of CN(I). Owing to the more negative conduction band position than the $O_2/{\bullet}O_2^-$ reduction potential, the photogenerated e^- can reduce and activate O_2 to form ${\bullet}O_2^-$. This process is followed by oxidation of ${\bullet}O_2^-$ into $^1O_2$ by h^+. Then, $^1O_2$ can selectively oxidize HMF to DFF. In addition, the valence band position of CN(I) is found to situate between the oxidation potentials required for HMF to DFF and DFF to byproducts. This band structure allows h^+ to directly oxidize HMF to DFF, too[10].

The stability and reusability of a heterogeneous catalyst are highly favored by potential industrial applications. Thereby, these crucial metrics of the Au/CN(I) photocatalyst were rigorously tested. The used catalyst was separated *via* filtration, thoroughly washed with ethanol and deionized water, and subsequently dried in an oven at 80 °C overnight. Figure 8C exhibits that the catalyst can maintain consistent performance across five successive cycles with minimal variations in HMF conversion and DFF selectivity. ICP-MS analysis of the post-reaction solution reveals the absence of Au component leached from the solid catalyst, validating the robust anchoring of Au by photodeposition on CN(I). TEM and XPS analyses further show the well preserved structure and morphology of this catalyst after reuses [Supplementary Figure 7]. These results can highlight the remarkable stability of Au/CN(I) photocatalysts.

CONCLUSIONS

In summary, highly-dispersed and small-sized Au nanoparticles deposited on *g*-C_3N_4 were shown as highly efficient photocatalysts for aerobic oxidation of HMF to DFF in water. The CN(I) carrier obtained by urea pyrolysis was disclosed to have a large specific surface area and a single-layered flake structure. The smaller Au nanoparticles (*ca.* 5.6 nm) enabled the strongest response of the catalyst for visible light. Moreover, Au nanoparticles on CN(I) excited by the LSPR effect allowed the generation of photoelectrons with sufficient energy to surpass the Schottky barrier. As a result, efficient separation and transfer of photogenerated e^- and h^+ were realized, leading to the highest productivity of DFF among benchmark catalysts. Furthermore, this study validated the generation and transformation of different reactive species during photocatalytic oxidation and identified h^+ and $^1O_2$ as catalytic active sites for the selective conversion of HMF to DFF. The cogenerated H_2O_2 as a byproduct *via* oxidation of HMF by $\bullet O_2^-$ radical can further oxidize DFF and even result in mineralization reaction. This work demonstrated for the first time the influence of relationship between LSPR effect and Schottky barrier on photocurrent and catalytic activity.

DECLARATIONS

Authors' contributions

Conceptualization, investigation, methodology, formal analysis, writing - original draft preparation: Zhang Q

Investigation, formal analysis: Fan B, Wang Y

Supervision, resources, funding acquisition: Gu B, Tang Q, Qiu F, Cao Q

Conceptualization, supervision, writing - review and editing, project administration, funding acquisition: Fang W

Availability of data and materials

Experimental details and supporting data can be found in Supplementary Materials. Other raw data that support the findings of this study are available from the corresponding author upon reasonable request.

Financial support and sponsorship

This work was supported by the National Natural Science Foundation of China (Nos. 22272149, 22062025), the Yunnan Fundamental Research Projects (Nos. 202201AU070095, 202301AT070169, 202401AV070020), the Yunnan University's Research Innovation Fund for Graduate Students (No. KC-23234000), and the Open Research Fund of School of Chemistry and Chemical Engineering of Henan Normal University.

Conflicts of interest

All authors declared that there are no conflicts of interest.

Ethical approval and consent to participate

Not applicable.

Consent for publication

Not applicable.

REFERENCES

1. Deng, W.; Wang, Y. Research perspectives for catalytic valorization of biomass. *J. Energy. Chem.* **2023**, *78*, 102-4. DOI
2. Deng, W.; Feng, Y.; Fu, J.; et al. Catalytic conversion of lignocellulosic biomass into chemicals and fuels. *Green. Energy. Environ.*

2023, *8*, 10-114. DOI

3. Li, Y.; Zhang, D.; Qiao, W.; et al. Nanostructured heterogeneous photocatalyst materials for green synthesis of valuable chemicals. *Chem. Synth.* **2022**, *2*, 9. DOI
4. Wen, H.; Zhang, W.; Fan, Z.; Chen, Z. Recent advances in furfural reduction via electro- and photocatalysis: from mechanism to catalyst design. *ACS. Catal.* **2023**, *13*, 15263-89. DOI
5. Wu, X.; Li, J.; Xie, S.; et al. Selectivity control in photocatalytic valorization of biomass-derived platform compounds by surface engineering of titanium oxide. *Chem* **2020**, *6*, 3038-53. DOI
6. Chen, S.; Wojcieszak, R.; Dumeignil, F.; Marceau, E.; Royer, S. How catalysts and experimental conditions determine the selective hydroconversion of furfural and 5-hydroxymethylfurfural. *Chem. Rev.* **2018**, *118*, 11023-117. DOI PubMed
7. Zhang, W.; Qian, H.; Hou, Q.; Ju, M. The functional and synergetic optimization of the thermal-catalytic system for the selective oxidation of 5-hydroxymethylfurfural to 2,5-diformylfuran: a review. *Green. Chem.* **2023**, *25*, 893-914. DOI
8. Zhang, Q.; Gu, B.; Fang, W. Sunlight-driven photocatalytic conversion of furfural and its derivatives. *Green. Chem.* **2024**, *26*, 6261-88. DOI
9. Wu, X.; Luo, N.; Xie, S.; et al. Photocatalytic transformations of lignocellulosic biomass into chemicals. *Chem. Soc. Rev.* **2020**, *49*, 6198-223. DOI
10. Zhang, Q.; Zhang, H.; Gu, B.; Tang, Q.; Cao, Q.; Fang, W. Sunlight-driven photocatalytic oxidation of 5-hydroxymethylfurfural over a cuprous oxide-anatase heterostructure in aqueous phase. *Appl. Catal. B.* **2023**, *320*, 122006. DOI
11. Wang, Y.; Gao, T.; Lu, Y.; Wang, Y.; Cao, Q.; Fang, W. Efficient hydrogenation of furfural to furfuryl alcohol by magnetically recoverable RuCo bimetallic catalyst. *Green. Energy. Environ.* **2022**, *7*, 275-87. DOI
12. Zhang, H.; Wang, Y.; Zhang, Q.; et al. Synergy in magnetic $Ni_xCo_1O_y$ oxides enables base-free selective oxidation of 5-hydroxymethylfurfural on loaded Au nanoparticles. *J. Energy. Chem.* **2023**, *78*, 526-36. DOI
13. Zhang, H.; Zhang, R.; Zhang, W.; et al. Base-free selective oxidation of 5-hydroxymethylfurfural over Pt nanoparticles on surface Nb-enriched Co-Nb oxide. Appl Catal B 2023;330:122670. DOI
14. Zhang, H.; Gao, T.; Zhang, Q.; et al. Synergistic catalysis in loaded PtRu alloy nanoparticles to boost base-free aerobic oxidation of 5-hydroxymethylfurfural. *Mater. Today. Catal.* **2023**, *3*, 100013. DOI
15. Fan, B.; Zhang, H.; Gu, B.; Qiu, F.; Cao, Q.; Fang, W. Constructing Pr-doped CoOOH catalytic sites for efficient electrooxidation of 5-hydroxymethylfurfural. *J. Energy. Chem.* **2025**, *100*, 234-44. DOI
16. Lilga, M. A.; Hallen, R. T.; Gray, M. Production of oxidized derivatives of 5-hydroxymethylfurfural (HMF). *Top. Catal.* **2010**, *53*, 1264-9. DOI
17. Deurzen MP, van Rantwijk F, Sheldon RA. Chloroperoxidase-catalyzed oxidation of 5-hydroxymethylfurfural. *J. Carbohydr. Chem.* **1997**, *16*, 299-309. DOI
18. Xia, T.; Gong, W.; Chen, Y.; et al. Sunlight-driven highly selective catalytic oxidation of 5-hydroxymethylfurfural towards tunable products. *Angew. Chem. Int. Ed. Engl.* **2022**, *61*, e202204225. DOI
19. Zhang, M.; Zhang, Y.; Ye, L.; et al. In situ fabrication $Ti_3C_2F_x$ MXene/$CdIn_2S_4$ schottky junction for photocatalytic oxidation of HMF to DFF under visible light. *Appl. Catal. B.* **2023**, *330*, 122635. DOI
20. Ismael, M.; Shang, Q.; Yue, J.; Wark, M. Photooxidation of biomass for sustainable chemicals and hydrogen production on graphitic carbon nitride-based materials: a comprehensive review. *Mater. Today. Sustain.* **2024**, *27*, 100827. DOI
21. Akhundi, A.; García-lópez, E. I.; Marcì, G.; Habibi-yangjeh, A.; Palmisano, L. Comparison between preparative methodologies of nanostructured carbon nitride and their use as selective photocatalysts in water suspension. *Res. Chem. Intermed.* **2017**, *43*, 5153-68. DOI
22. Wang, X.; Meng, S.; Zhang, S.; Zheng, X.; Chen, S. 2D/2D MXene/g-C_3N_4 for photocatalytic selective oxidation of 5-hydroxymethylfurfural into 2,5-formylfuran. *Catal. Commun.* **2020**, *147*, 106152. DOI
23. Krivtsov, I.; García-lópez, E. I.; Marcì, G.; et al. Selective photocatalytic oxidation of 5-hydroxymethyl-2-furfural to 2,5-furandicarboxyaldehyde in aqueous suspension of g-C_3N_4. *Appl. Catal. B.* **2017**, *204*, 430-9. DOI
24. Ilkaeva, M.; Krivtsov, I.; García, J. R.; et al. Selective photocatalytic oxidation of 5-hydroxymethyl-2-furfural in aqueous suspension of polymeric carbon nitride and its adduct with H_2O_2 in a solar pilot plant. *Catal. Today.* **2018**, *315*, 138-48. DOI
25. Ilkaeva, M.; Krivtsov, I.; García-lópez, E.; et al. Selective photocatalytic oxidation of 5-hydroxymethylfurfural to 2,5-furandicarboxaldehyde by polymeric carbon nitride-hydrogen peroxide adduct. *J. Catal.* **2018**, *359*, 212-22. DOI
26. Marcì, G.; García-lópez, E.; Pomilla, F.; et al. Photoelectrochemical and EPR features of polymeric C_3N_4 and O-modified C_3N_4 employed for selective photocatalytic oxidation of alcohols to aldehydes. *Catal. Today.* **2019**, *328*, 21-8. DOI
27. Mao, Q.; Ma, J.; Chen, M.; Lin, S.; Razzaq, N.; Cui, J. Recent advances in heavily doped plasmonic copper chalcogenides: from synthesis to biological application. *Chem. Synth.* **2023**, *3*, 26. DOI
28. Lee, S.; Lee, S. W.; Jeon, T.; Park, D. H.; Jung, S. C.; Jang, J. Efficient direct electron transfer via band alignment in hybrid metal-semiconductor nanostructures toward enhanced photocatalysts. *Nano. Energy.* **2019**, *63*, 103841. DOI
29. Furube, A.; Du, L.; Hara, K.; Katoh, R.; Tachiya, M. Ultrafast plasmon-induced electron transfer from gold nanodots into TiO_2 nanoparticles. *J. Am. Chem. Soc.* **2007**, *129*, 14852-3. DOI PubMed
30. Fowler, R. H. The analysis of photoelectric sensitivity curves for clean metals at various temperatures. *Phys. Rev.* **1931**, *38*, 45-56. DOI
31. Liu, Y.; Chen, Q.; Cullen, D. A.; Xie, Z.; Lian, T. Efficient hot electron transfer from small Au nanoparticles. *Nano. Lett.* **2020**, *20*,

4322-9. DOI

32. Yang, Q.; Wang, T.; Han, F.; Zheng, Z.; Xing, B.; Li, B. Bimetal-modified g-C_3N_4 photocatalyst for promoting hydrogen production coupled with selective oxidation of biomass derivative. *J. Alloys. Compd.* **2022**, *897*, 163177. DOI
33. Ghalta, R.; Srivastava, R. Photocatalytic selective conversion of furfural to γ-butyrolactone through tetrahydrofurfuryl alcohol intermediates over Pd NP decorated g-C_3N_4. *Sustain. Energ. Fuels.* **2023**, *7*, 1707-23. DOI
34. Kresse, G.; Furthmüller, J. Efficiency of ab-initio total energy calculations for metals and semiconductors using a plane-wave basis set. *Comp. Mater. Sci.* **1996**, *6*, 15-50. DOI
35. Xiong, T.; Cen, W.; Zhang, Y.; Dong, F. Bridging the g-C_3N_4 interlayers for enhanced photocatalysis. *ACS. Catal.* **2016**, *6*, 2462-72. DOI
36. Wang, X.; Maeda, K.; Thomas, A.; et al. A metal-free polymeric photocatalyst for hydrogen production from water under visible light. *Nat. Mater.* **2009**, *8*, 76-80. DOI
37. Fang, W.; Fan, Z.; Shi, H.; et al. Aquivion®-carbon composites via hydrothermal carbonization: amphiphilic catalysts for solvent-free biphasic acetalization. *J. Mater. Chem. A.* **2016**, *4*, 4380-5. DOI
38. Wu, S.; Shang, R.; Zhang, H.; et al. Steering the Au-$Fe_xCo_1O_y$ interface for efficient imine synthesis at low temperature via oxidative coupling reaction. *Mol. Catal.* **2023**, *547*, 113292. DOI
39. García-lópez, E. I.; Pomilla, F. R.; Bloise, E.; et al. C_3N_4 impregnated with porphyrins as heterogeneous photocatalysts for the selective oxidation of 5-hydroxymethyl-2-furfural under solar irradiation. *Top. Catal.* **2021**, *64*, 758-71. DOI
40. Movahed, S. K.; Miraghaee, S.; Dabiri, M. AuPd alloy nanoparticles decorated graphitic carbon nitride as an excellent photocatalyst for the visible-light-enhanced Suzuki-miyaura cross-coupling reaction. *J. Alloys. Compd.* **2020**, *819*, 152994. DOI
41. Lu, G.; Chu, F.; Huang, X.; Li, Y.; Liang, K.; Wang, G. Recent advances in metal-organic frameworks-based materials for photocatalytic selective oxidation. *Coord. Chem. Rev.* **2022**, *450*, 214240. DOI
42. Xu, S.; Zhou, P.; Zhang, Z.; et al. Selective oxidation of 5-hydroxymethylfurfural to 2,5-furandicarboxylic acid using O_2 and a photocatalyst of Co-thioporphyrazine bonded to g-C_3N_4. *J. Am. Chem. Soc.* **2017**, *139*, 14775-82. DOI
43. Peng, D.; Zhang, Y.; Xu, G.; Tian, Y.; Ma, D.; Zhang, Y. Novel p-n heterojunctions incorporating $NiS_{1.03}$@C with nitrogen doped TiO_2 for enhancing visible-light photocatalytic performance towards cyclohexane oxidation. *Appl. Surf. Sci.* **2021**, *566*, 150676. DOI
44. Yang, M. Q.; Zhang, N.; Xu, Y. J. Synthesis of fullerene-, carbon nanotube-, and graphene-TiO_2 nanocomposite photocatalysts for selective oxidation: a comparative study. *ACS. Appl. Mater. Interf.* **2013**, *5*, 1156-64. DOI
45. Zhang, M.; Yu, Z.; Xiong, J.; Zhang, R.; Liu, X.; Lu, X. One-step hydrothermal synthesis of $Cd_xIn_yS_{(x+1.5y)}$ for photocatalytic oxidation of biomass-derived 5-hydroxymethylfurfural to 2,5-diformylfuran under ambient conditions. *Appl. Catal. B.* **2022**, *300*, 120738. DOI

Qizhao Zhang

Qizhao Zhang is currently pursuing a PhD in physical chemistry at Yunnan University under the supervision of Prof. Wenhao Fang. Before embarking on his doctoral journey, he obtained a BSc degree from Fuzhou University, laying a solid academic foundation for his research career. His research interests cover the crucial area of biomass conversion through photocatalysis with a specific emphasis on the low-carbon utilization of lignocellulosic biomass. Recently, his work has centered on the visible-light-driven photooxidation of furan compounds in water medium to various chemicals using synergistic hybrid catalysts with unique configurations. To date, he has co-authored six SCI papers.

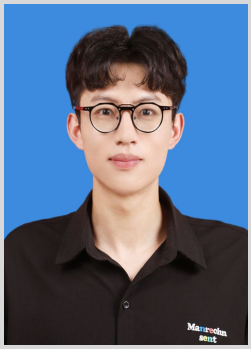

Botao Fan

Botao Fan is currently pursuing a master's degree in physical chemistry at Yunnan University, where he has been studying under the tutelage of Prof. Wenhao Fang since 2022. Prior to this, he obtained a bachelor's degree in applied chemistry from Sichuan Agricultural University (2017-2021). His research focuses on the design, preparation and characterization of particular morphology catalytic materials for biomass conversion. He is committed to the eletcro- and/or photo-chemical upgrading of furfural platform molecules to valuable and sustainable building block chemicals and further to unveiling the structure-activity relationship at the catalytic interface by using in situ techniques and theoretical tools.

Yuxi Wang

Yuxi Wang obtained his bachelor's degree in chemistry from Hanjiang Normal University in 2023. He has been pursuing a master's degree in physical chemistry at Yunnan University since 2023 under the supervision of Prof. Wenhao Fang. His research focuses on the selective photoreduction of furfural biomass platform molecules into chemicals using semiconductor catalytic materials.

Bang Gu

Bang Gu received his PhD in 2019 from the University of Lille, where he conducted research under the supervision of Andrei Khodakov. He joined Yunnan University in 2021 as an associate professor and was recognized as one of the Xingdian Outstanding Young Talents of Yunnan Province in 2022. He is currently serving as the Director of Chemistry at Yunnan University. His research focuses on heterogeneous catalysis for energy-related processes, including Fischer-Tropsch synthesis, biomass conversion, photocatalytic transformation of biomass platform molecules and oxidative coupling of methane.

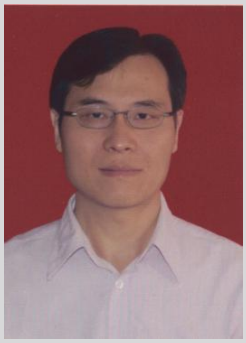

Qinghu Tang

Prof. Qinghu Tang received his PhD in physical chemistry from Xiamen University, China. Since 2011, he has been a distinguished professor of physical chemistry in Henan Province at Henan Normal University, China. His current research interests include heterogeneous catalysis, selective oxidation, and catalytic application of nano-carbon materials.

Feng Qiu

Feng Qiu received his PhD in microelectronics and solid-state electronics from the Shanghai Institute of Technology Physics, Chinese Academy of Sciences, in 2013. In 2014, he joined Fudan University as a senior visiting scholar. Currently, he is a full associate professor at Yunnan University, studying low-dimensional photoelectric material, its photovoltaic devices, and photodetectors as the leader of the Yunnan University Key Laboratory for Optoelectronics and Microelectronics.

Qiue Cao

Qiue Cao has been a full professor in chemistry at Yunnan University since 2001. She obtained her PhD in analytical chemistry from Lanzhou University in 1999 and currently serves as the Head of the School of Chemical Science and Technology. Her research interests include separation science, electrochemical sensors, molecular imprinting techniques, and capillary electrophoresis. She is a member of the Advisory Board of Metallurgical Analysis (2006), a member of the Advisory Board of the Chinese Journal of Analysis Laboratory (2012), Vice Chairman of the Food Expert Committee of the Food and Drug Administration of Yunnan Province (2015), and Vice Chairman of the Expert Committee of Plastics Industry Association of Yunnan Province (2015).

Wenhao Fang

Wenhao Fang obtained his bachelor's and master's degrees in chemistry and physical chemistry from Xiamen University in 2007 and 2010, respectively. He then earned his PhD in Molécules et Matière Condensée from Université de Lille in 2013. Following this, he worked as a postdoc fellow of industrial catalysis at UMI 3464 CNRS/Solvay (2013-2015). In 2015, he joined Yunnan University as an Associate Professor and established the Group of Green Catalysis and Low-Carbon Conversion in 2017. He was promoted to full professor and appointed as a PhD advisor in 2020. His major research interests include catalytic biomass conversion, catalyst development, energy catalysis and green chemistry. As an expert in heterogeneous catalysis, he has authored over 60 peer-reviewed publications and holds 20 granted Chinese patents. He serves on the editorial board of Molecular Catalysis as an early career member, a position he has held since 2024.